# Electrostatic capacitance-type acceleration of ions with an intense few-cycle laser pulse

**Published in:**
Applied Physics Letters

**Document Version:**
Peer reviewed version

**Queen's University Belfast - Research Portal:**
Link to publication record in Queen's University Belfast Research Portal

# Electrostatic Capacitance-type Acceleration of Ions with an Intense Few-Cycle Laser Pulse

X. F. Shen,[1,2] B. Qiao,[1,2,a)] H. Zhang,[1,3] Y. Xie,[1,2] S. Kar,[4] M. Borghesi,[4] M. Zepf,[5] C. T. Zhou,[1,3] S. P. Zhu,[6] and X. T. He[1,2,6]

[1)]*Center for Applied Physics and Technology, HEDPS, SKLNPT, and School of Physics, Peking University, Beijing, 100871, China*

[2)]*Collaborative Innovation Center of IFSA, Shanghai Jiao Tong University, Shanghai 200240, China*

[3)]*Shenzhen Technology University, Shenzhen 518118, China*

[4)]*Center for Plasma Physics, School of Mathematics and Physics, Queen's University Belfast, Belfast BT7 1NN, UK*

[5)]*Helmholtz Institut Jena, Frbelstieg 3, 07743 Jena, Germany*

[6)]*Institute of Applied Physics and Computational Mathematics, Beijing 100094, China*

(Dated: 25 March 2019)

We use large scale, three-dimensional particle-in-cell simulations to demonstrate that a high-quality energetic ion beam can be stably generated by irradiation of a multi-species nanofoil target with an intense few-cycle laser pulse. In this scheme, named "electrostatic capacitance-type acceleration", the light ions of the nanofoil are accelerated by a uniform capacitor-like electrostatic field induced by the laser-blown-out electrons that act like the cathode of a capacitor, while the heavy ions left behind serve as the anode. This scheme overcomes the inherent obstacles existing in the other acceleration mechanisms, such as uncontrollability of target normal sheath acceleration and instability of radiation pressure acceleration. Theoretical studies and three-dimensional particle-in-cell simulations show that this acceleration scheme is much more stable and efficient than previous, by which 100MeV monoenergetic proton beams (energy spread $< 10\%$) can be obtained with laser energy less than 10J, and GeV ones with about 100J.

PACS numbers: 52.38.Kd, 41.75.Jv, 52.38.-r, 52.27.Ny

Laser-driven ion acceleration is expected to be a new generation of advanced accelerators[1,2] for production of compact high-energy ion sources with unique properties, such as extreme laminarity and large flux. Prospective applications include proton radiography[3], tumor therapy[4], and nuclear physics[5]. However, most applications require generation of the ion beam with high energy ($>100$MeV) and small energy spread ($< 10\%$), which has not been achieved yet and, in fact, is extremely challenging for the existing acceleration mechanisms[6–10].

To date, two main mechanisms have been identified and widely investigated in both theory and experiments: target normal sheath acceleration (TNSA) and radiation pressure acceleration (RPA). In TNSA[11–14], linearly-polarized (LP) laser pulses are used to irradiate micrometer-scale targets, in which ions are accelerated by the electrostatic sheath field arising from thermal expansion of hot electrons generated by the $\boldsymbol{J} \times \boldsymbol{B}$ heating in front of the target, where the thermal pressure dominates. This thermal expansion process is intrinsic and robust, which makes TNSA easily accessible in experiments, but also uncontrollable, leading to a broad energy spectrum, low efficiency, and an unfavorable scaling for ion energy as a function of laser intensity as $E_i \propto I^{1/2}$. In RPA[15–22], circularly-polarized (CP) laser pulses are used to irradiate nanometer-scale targets. Ions and electrons constituting a quasineutral plasma slab undergo synchronous acceleration directly by laser radiation pressure, which yields

higher efficiency, smaller energy spread and more promising scaling as $E_i \propto I$. Nevertheless, such synchronous acceleration is largely based on the dynamic balance between plasma charge separation potential and light pressure, which is very susceptible to the interface instabilities[16,23]. In practical experiments[8,19,21], the acceleration generally breaks prematurely, where the achievable ion energy is rather limited and the beam quality is heavily destroyed.

Besides the remarkable efforts devoted to the advancement of laser technology and targetry to improve the quality of laser-accelerated ion beams, the development of novel acceleration mechanisms may provide an alternative approach. On the other hand, the rapid progress of laser technology, in particular, intense few-cycle lasers[24–29], has necessarily brought novel mechanisms[30,31]. For example, the Light wave synthesizer 20[32] delivers laser pulses with intensity $1.3 \times 10^{20}$W/cm$^2$ and pulse duration 5.1fs, and the Petawatt field synthesizer (PFS)[26] under construction aims at 5J in 5fs ($<2$cycle).

In this Letter, we propose a scheme, named "electrostatic capacitance-type acceleration" (ECA), which is able to overcome the above obstacles from its essence and suitable for few-cycle laser devices. The acceleration process relies on the formation of an electrostatic capacitor by using a multi-species nanofoil target irradiated with an intense few-cycle laser in the blown-out regime, i.e., the radiation pressure much larger than the electrostatic pressure, which can be divided into two stages, shown as Fig. 1. Firstly, because of the small areal density, the target is punched through directly. All nanofoil electrons are blown-out and accelerated forward quickly by the intense laser, forming a flying electron sheet
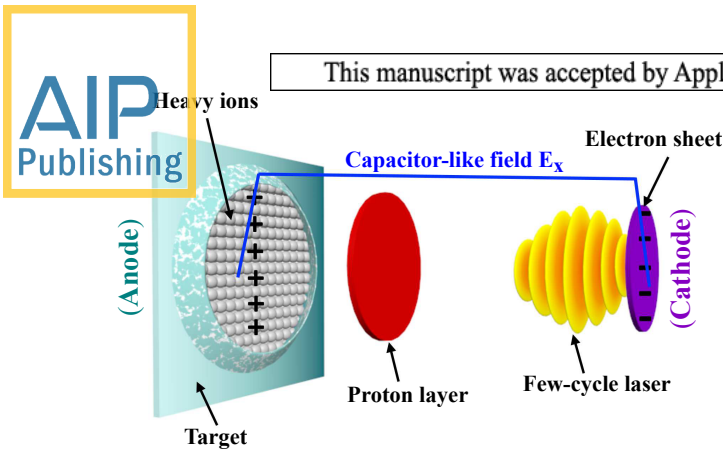
FIG. 1. (color online) Schematic of the ECA scheme, where a multi-species nanofoil target is irradiated by an intense few-cycle laser (yellow). The protons (red) of nanofoil are accelerated by a uniform capacitor-like electrostatic field $E_x$ (blue) induced by laser-blown-out electrons (purple) that act like the cathode of a capacitor, while heavy ions (green) left behind serve as the anode.

that acts like the cathode of a capacitor, while the heavy ions left behind serve as an anode of the capacitor. Meanwhile, the laser energy is transformed into the electrostatic potential stored in the capacitor, like the capacitor charging stage. Afterwards, the light ions (protons) of the nanofoil are accelerated by the uniform electrostatic field between two nodes of the capacitor, during which the electrostatic potential energy is transferred to ion energy, like capacitor discharging. Because the charging and discharging stages are separated, which, different from RPA, does not need to keep the dynamic balance between the light and electrostatic pressures during acceleration, the ECA is rather stable and controllable, resulting in production of high-energy monoenergetic ion beams. Our theoretical studies have given the required laser and target conditions for this scheme, and shown that the ion peak energy scales as a function of laser energy as $E_i \propto \xi_L$ in the weak relativistic regime and $E_i \propto \sqrt{\xi_L}$ in the ultrarelativistic limit. Large scale, three-dimensional (3D) particle-in-cell (PIC) simulations have verified the theory and shown that monoenergetic proton beams with peak energy $> 100$MeV can be obtained at laser energy $\xi_L \sim 10$J and GeV with $\xi_L \sim 100$J.

To get insight into the ECA dynamics, we start from single electron motion equations under laser fields $\mathbf{E}$ and $\mathbf{B}$ as well as the capacitor-like electrostatic field $\mathbf{E}_x$ along x-direction as $d\mathbf{p}/dt = -e(\mathbf{E} + \mathbf{v} \times \mathbf{B}) - e\mathbf{E}_x$ and $d\gamma/dt = -e(\mathbf{v} \cdot \mathbf{E} + \mathbf{v} \cdot \mathbf{E}_x)/m_e c^2$, where $\mathbf{p} = \gamma m_e \mathbf{v}$ and $\gamma = (1 + p^2/m_e^2 c^2)^{1/2}$ are the electron momentum and relativistic factor, respectively. The CP laser is assumed to propagate along x-direction with normalized vector potential $\mathbf{A} = a[\cos(\omega_L \tau)\mathbf{e_y} + \sin(\omega_L \tau)\mathbf{e_z}]$ and $a = a_0 \sin(\pi\tau/\tau_L)$ for $0 < \tau < \tau_L$ and $a = 0$ for $\tau > \tau_L$, where $\tau = t - x/c$, $a_0 = (0.85/\sqrt{2})(I\lambda^2/10^{18}\text{Wcm}^{-2}\mu\text{m}^2)^{1/2}$, $\omega_L$ and $\tau_L$ are laser frequency and pulse duration. The assumption of the parallel-plate capacitor model is also taken so that $\mathbf{E}_x = E_c\mathbf{e_x}$. Assuming the electron to be initially at rest, after some algebra, we obtain the electron motion equation in the

transverse and longitudinal directions, respectively, as

$$\mathbf{p}_\perp = e\mathbf{A}, \tag{1}$$

$$\frac{dp_x}{dt} = \frac{1}{R}\frac{e^2 a}{m_e c}\frac{da}{dt} - eE_c, \tag{2}$$

$$R = \gamma - \frac{p_x}{m_e c} = 1 + \frac{eE_c}{m_e c}\int d\tau, \tag{3}$$

where $R$ represents the dephasing rate[33]. Eqs. (1)-(3) together describe the motion of the blown-out electrons from a multi-species nanofoil by lasers, which serve as the cathode of a capacitor in ECA. Here the role of $E_c$ is not only directly slowing down electron acceleration, but also is linked with the laser ponderomotive force through the dephasing rate $R$ ($R > 1$), which both result in deceleration and eventually turning back of the blown-out electrons.

When the electron turns backward at $\tau_b = t_b - x_b/c$, the longitudinal momentum $p_{xb} = 0$. Substituting $\gamma^2 = 1 + (p_\perp^2 + p_x^2)/m_e^2 c^2$ into Eq. (3), we easily get that

$$\frac{p_{xb}}{m_e c} = \frac{1 + a_0^2 \sin^2(\pi\tau_b/\tau_L) - R^2}{2R} = 0. \tag{4}$$

Further assuming all nanofoil electrons are blown-out quickly, we get $E_c \approx 4\pi n_e el$. From Eqs. (3) and (4), we obtain the optimal condition of laser and foil parameters for the ECA scheme

$$\frac{\tau_L}{T_0} \approx \frac{a_0}{4\pi(n_e/n_c)(l/\lambda)}, \tag{5}$$

with $T_0 = 2\pi/\omega_L$ and $n_c = \pi m_e c^2/e^2\lambda^2$, which is not only related to the target areal density, but also the pulse duration. This condition ensures radiation pressure is much larger than electrostatic pressure, which means the target thickness required for ECA is smaller than that for RPA at the same laser intensity[17,18]. Meanwhile, from the ion motion equation $dp_i/dt = eE_c$, we can estimate the maximum ion energy as

$$\frac{p_i}{m_i c} = a_0 \frac{m_e}{m_i}\frac{\pi x_b}{c\tau_L}. \tag{6}$$

From Eqs. (5) and (6), we conclude that, the ECA prefers few-cycle laser pulses, which means higher ion energies can be obtained with shorter durations, or more generally with steeper rising front of laser pulses [Eq. (2)]. Moreover, the condition to evacuate electrons completely from solid targets has always been determined from simulation results[31,34], here we derive its specific expression from theory and reveal its relationship with pulse duration [Eq. (5)].

To prove the above theory, 1D PIC simulations are firstly performed using the EPOCH code[35]. A CP laser propagating from the left boundary at $x = -20\lambda$ with $a_0 = 54$ and $\lambda = 800$nm is incident on a diamondlike carbon (DLC) nanofoil at $x = 0$, whose electron density is $n_e = 385n_c$ and thickness $l = 4$nm. The target is assumed to be fully-ionized initially since the laser intensity is much larger than the ionization potential of carbon ions[36]. The proton ($H^+$) to carbon ion ($C^{6+}$) density ratio is $n_{ip} : n_{ic} = 1 : 9$. The laser pulse is temporally sinusoidal with duration varying from $\tau_L = 1$ to $3T_0$.
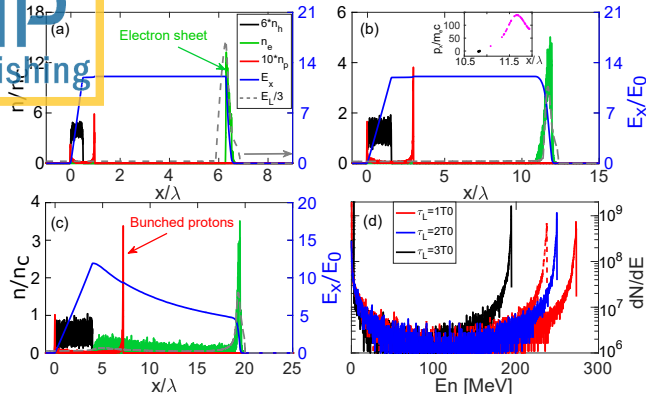
FIG. 2. (color online) 1D PIC simulation results: the density profiles of carbon ions ($n_c$, black), protons ($n_p$, red) and electrons ($n_e$, green) as well as longitudinal profiles of accelerating field ($E_x$, blue) and laser field ($E_L$, dashed grey) at $t = 7$ (a), 12.5 (b) and $20T_0$ (c), respectively, where a one-cycle ($\tau_L = T_0$) CP laser of $a_0 = 54$ is irradiating a DLC nanofoil of $l = 4$nm. The inset of (b) shows the electron phase space $(x, p_x)$, in which the black dots show the backward electrons ($p_x < 0$). (d) Energy spectra of protons at $t = 20T_0$ for pulse duration of respectively $\tau_L = T_0$ (red), $2T_0$ (blue) and $3T_0$ (black). The dashed red line in (d) represents the spectrum with one-cycle LP laser.

Figures 2(a)-2(c) show evolutions of respectively electron $n_e$ (green) and ion (black for carbon $n_c$ and red for proton $n_p$) density profiles, as well as the longitudinal profiles of accelerating field $E_x$ (blue) and laser field $E_L$ (dashed grey) at $t = 7$, 12.5 and $20T_0$ for the case $\tau_L = 1T_0$. During the charging stage [Fig. 2(a)], all nanofoil electrons are blown out and pushed forward without heating by laser ponderomotive force, forming a dense flying electron sheet. Between this electron sheet (like a cathode) and the left nanofoil ions (like an anode), a uniform capacitor-like electrostatic field $E_x$ develops. Afterwards, due to larger charge-to-mass ratio, preferentially protons are accelerated homogeneously by this capacitor electric field until they encounter the backward electrons, shown as the black dots in inset of Fig. 2(b). When a significant number of electrons turn backward ($p_x < 0$) [Fig. 2(c)], $E_x$ decreases and evolves into a profile with a negative gradient. The proton acceleration becomes slower, but still keeps bunching (even compressed), because fast protons in front experience weaker $E_x$ acceleration while slow protons behind under stronger $E_x$. Therefore, a high-quality energetic proton beam can be obtained and maintained for a long time in ECA, where the proton energy spectrum at $t = 20T_0$ is shown by the red solid line in Fig. 2(d). For $\tau_L$ varying from 1 to $3T_0$, simulations show that the time when the first electron turns backward is shifted earlier from $12.5T_0$ to $6.75T_0$, within our expectation [Eq. (2)]. Proton energy spectra for $\tau_L = 2$ (blue) and $3T_0$ (black) are also plotted in Fig. 2(d), which clearly show that protons obtain higher energy by using shorter pulse duration, coinciding with Eq. (6).

To show that the ECA scheme is not a 1D artefact, large-scale 3D PIC simulations are run. The laser intensity keeps the same as 1D and the pulse profile is Gaussian distributed in

both space and time with diameter $d_L = 10\mu$m (full width at half maximum (FWHM) in intensity) and $\tau_L = 8$fs (FWHM). Due to limitation of computational resources, we reduce the electron density as $n_e = 64n_c$ but increase its thickness as $l = 18$nm, so that keeping the same areal density[19]. Moreover, a transverse mass-limit-target (its transverse size is comparable to $d_L$) is used to avoid reduction of the longitudinal electrostatic field caused by the electron returning from the transverse edge. The simulation box size is $45.6\mu$m $\times 30\mu$m $\times 30\mu$m, composed of $7600 \times 1300 \times 1300$ grids. 400 particles per cell for each species are taken. The convolutional perfectly matched layer boundary conditions[37] are used.

Figures 3(a) and 3(b) show isosurface plots of electron and ion densities at $t = 5$ and $32T_0$ respectively. They together clearly demonstrate the dynamics of ECA in both charging and discharging stages, where protons (red) are firstly accelerated by the uniform $E_x$ (blue) and later by a bunching one with negative gradient since electrons (purple) turn backward. Because of finite spot size, the turning backward of electrons occurs firstly from the transverse edge and then to the center [Fig. 3(b)]. Eventually, a monoenergetic proton beam with peak energy 76MeV and energy spread only 8% is obtained [solid red line in Fig. 3(c)], which proves that the effects of instabilities are not prominent in ECA even in 3D cases, unlike that in RPA. This is because that, on the one hand, in ECA the dynamic balance between the light and electrostatic pressure does not need to keep; on the other hand, the few-cycle pulse duration here may also be too short for instabilities to grow sufficiently. What's more, this narrow energy spectrum feature can be kept even for time much longer than the simulation window. A 3D PIC simulation with laser parameters same as the PFS ($\xi_L = 5$J, $\tau_L = 5$fs and $d_L = 6\mu$m) is also performed, which shows that a monoenergetic proton beams with peak energy $\sim 45$MeV is obtained and also verifies the potential in ion acceleration for few-cycle laser devices.

Now, let's discuss the scaling of ion energy in ECA. Since in a realistic multidimensional situation the laser has a finite spot size $d_L$, the above theory and 1D simulations actually overestimate the final ion energy. This is because the assumption of parallel-plate capacitor model becomes invalid when the blown-out electron sheet (cathode) is accelerated over a distance $d > d_L$, where the electrostatic field significantly decreases and acceleration efficiency heavily drops. To give the ion energy scaling, here we estimate the effective ion acceleration distance as $x_b \approx d_L$. From Eq. (6), in the weak relativistic regime we easily obtain the final peak ion energy scales as $\xi_i \approx 23.6\xi_L/(\tau_L/T_0)$[MeV], while in the ultrarelativistic limit, $\xi_i \approx 210.6\sqrt{\xi_L/(\tau_L/T_0)}$[MeV]. Therefore, we conclude that in ECA, the peak ion energy scales as the laser energy as $\xi_i \sim \xi_L$ in the weak relativistic regime and $\xi_i \sim \sqrt{\xi_L}$ in the ultrarelativistic limit, which means that higher ion energy can be obtained with larger laser energy. These scalings are much stronger than those of RPA, which are actually related to the pulse fluence and large laser spots are required[10,18].

To verify the scalings, a series of 2D simulations are performed, since 3D simulations need too large amounts of computer resources and the inherent physics is analogous to 2D. The laser energy varies from 1J to 1000J by ten typical cases
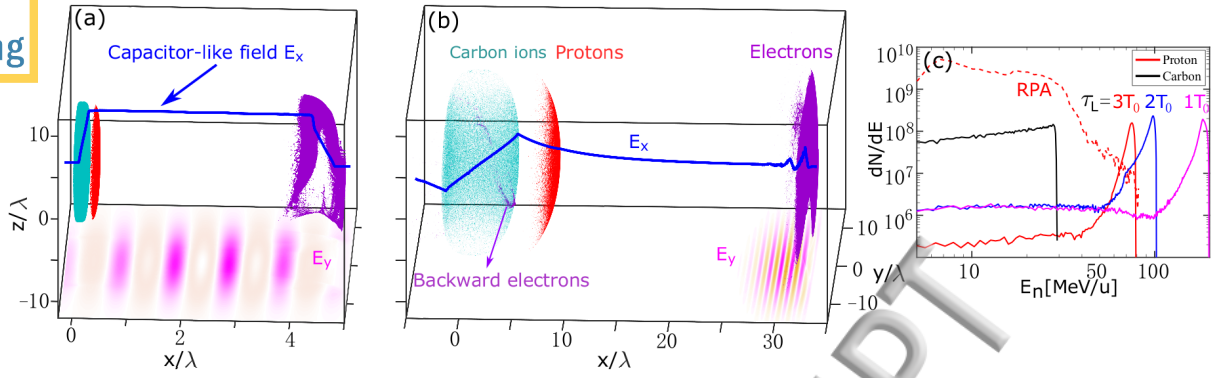
FIG. 3. (color online) 3D PIC simulation results: evolutions of the density isosurfaces for carbon ions (cyan), protons (red) and electrons (magenta) at $t = 5$ (a) and $32T_0$ (b), where a CP laser with $a_0 = 54$, $d_L = 10\mu$m and $\tau_L = 3T_0$ is used. The blue lines represent the longitudinal electric field $E_x$ near x-axis. (c) energy spectra of carbon ions (solid black) and protons (solid red) within $r < 4\mu$m. The red dashed line represents the proton energy spectrum from RPA with the same laser parameters and the corresponding optimal foil thickness ($l = 230$nm)[18]. The blue and purple lines show the proton energy spectra achieved with pulse duration $\tau_L = 2T_0$ and $1T_0$, respectively.
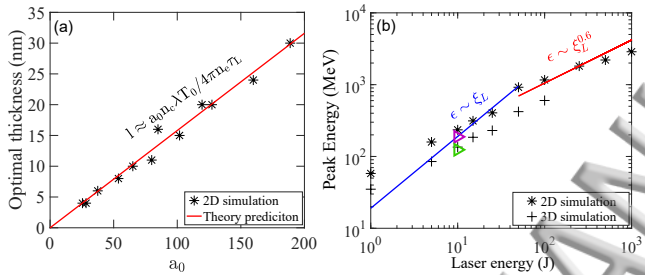


FIG. 4. (color online) Simulation results for the scaling. (a) The optimal foil thickness $l$ versus $a_0$, where black asterisks show those got from simulations and the red line is from Eq. (5). (b) The peak proton energy $\varepsilon_i$ (black asterisks) vs laser energy $\xi_L$ varying from 1J to 1000J under the optimal condition. The blue and red lines show the fitting of simulation results. The laser energies and focal radii are respectively (1J, 2$\mu$m), (5J, 2.5$\mu$m), (10J, 3$\mu$m), (15J, 3$\mu$m), (25J, 3.6$\mu$m), (50J, 3$\mu$m), (100J, 4$\mu$m), (250J, 5$\mu$m), (500J, 7$\mu$m) and (1000J, 9$\mu$m). The green triangle represents the peak proton energy of a LP laser with (10J, 3$\mu$m). And the purple one, plotted in the same value of coordinate $x$ to conveniently compare with other cases, shows the result of a long laser pulse (actually much larger laser energy with other parameters unchanged), where a "shutter" for steepening the rising front of laser is used. Further, the black crosses show those obtained from 3D simulations.

(1J, 5J, 10J, 15J, 25J, 50J, 100J, 250 J, 500J and 1000J). The laser pulse is temporally and transversely Gaussian, similar to that in 3D. The spot size and the intensity of lasers vary simultaneously to verify the scaling, and, meanwhile, to also confirm the robustness of the scheme with small laser spot sizes down to radius of 2$\mu$m. Note that though the maximum intensity here is $1.35 \times 10^{23}$W/cm$^2$, the radiation reaction effect could be ignored, as electrons move in almost the same direction as the laser propagation direction in most of acceleration time and when they turn backward, their energies and the laser field they felt are very small[38]. The target parameters are similar to those in 1D simulations.

Figure 4(a) shows the parameter scan for the optimal nanofoil thickness $l$ varying with different laser amplitude $a_0$ got from a series of 2D simulations (asterisks). Obviously the results agree well with the theoretical estimation (red line) from Eq. (5). With Eq. (5) satisfied, Fig. 4(b) proves that the final peak ion energy increases almost linearly with laser energy as $\xi_i \sim \xi_L$ in the weak relativistic regime, which is consistent with the theory above. The ion energy $\xi_i$ can reach 1GeV with only $\xi_L \sim 50$J, an order of magnitude lower than that required by RPA[15,17,39]. When the ion energy is larger than 1GeV, the relativistic effect sets in and the scaling decreases to $\xi_i \propto \xi_L^{0.6}$. As the computational cost increases dramatically with laser energies, only several 3D simulations for this scaling study are carried out, whose results are shown by the black crosses in Fig. 4(b). They prove that the linear scaling law is still valid in 3D, though the ion peak energies are comparatively lower than those in 2D, in consistence with that in Ref.[40]. More importantly, when laser energy is about 10J, a monoenergetic ion beam with peak energy about 130MeV (energy spread 8%) is obtained, which has not been achieved by RPA and/or other mechanisms yet in either experiments or simulations under the same $\xi_L$. Also note that from Fig. 4(b), we see that the ECA scheme is rather robust even for the spot size as small as radius of 2$\mu$m.

In summary, a scheme for achieving high-quality energetic ion beams, namely, "electrostatic capacitance-type acceleration" (ECA), by irradiation of a multi-species nanofoil target with an intense few-cycle laser pulse is proposed. This scheme is rather stable and efficient, which can also be used to accelerate heavy ions, such as carbon ions, only if a heavier ion substrate acts as the anode. Meanwhile, the acceleration keeps much longer and more efficient with an intense few-cycle CP laser pulse. Though circular-polarization is preferable, the ECA scheme also works with a LP laser, except that the obtained ion energy is slightly lower [see the green triangle point in Fig. 4(b)]. More importantly, for comparatively long pulses, for example, 25fs (about 9 cycles), 2D simulations [purple triangle in Fig. 4(b)] show that this scheme still

works by using a "shutter"[41,42] to steepen the laser rising front [Eq. (2)]. Note that in the latter case, the laser energy is actually much larger than 10J as the other laser parameters keep unchanged. Here we plot these cases in the same value of the coordinate $x$ to conveniently compare their peak energies.

[1] A. Macchi, M. Borghesi, and M. Passoni, Rev. Mod. Phys. **85**, 751 (2013).

[2] H. Daido, M. Nishiuchi, and A. S. Pirozhkov, Rep. Prog. Phys. **75**, 056401 (2012).

[3] M. Borghesi, A. Schiavi, D. H. Campbell, M. G. Haines, O. Willi, A. J. MacKinnon, L. A. Gizzi, M. Galimberti, R. J. Clarke and H. Ruhl, Plasmas Phys. Control. Fusion **43**, A267 (2001).

[4] S. V. Bulanov, T. Z. Esirkepov, V. S. Khoroshkov, A. V. Kuznetsov, and F. Pegoraro, Phys. Lett. A **299**, 240 (2002).

[5] F. N. Beg, K. Krushelnick, C. Gower, S. Torn, A. E. Dangor, A. Howard, T. Sumner, A. Bewick, V. Lebedenko, J. Dawson et al., Appl. Phys. Lett. **80**, 3009 (2002).

[6] F. Wagner, O. Deppert, C. Brabetz, P. Fiala, A. Kleinschmidt, P. Poth, V. A. Schanz, A. Tebartz, B. Zielbauer, M. Roth et al., Phys. Rev. Lett. **116**, 205002 (2016).

[7] M. Nakatsutsumi, Y. Sentoku, A. Korzhimanov, S. N. Chen, S. Buffechoux, A. Kon, B. Atherton, P. Audebert, M. Geissel, L. Hurd et al., Nat. Commun. **9**, 280 (2018).

[8] A. Higginson, R. J. Gray, M. King, R. J. Dance, S. D. R. Williamson, N. M. H. Butler, R. Wilson, R. Capdessus, C. Armstrong, J. S. Green et al., Nat. Commun. **9**, 724 (2018).

[9] X. F. Shen, B. Qiao, H. Zhang, Y. Xie, C. T. Zhou, S. P. Zhu, and X. T. He, e-print arXiv:physics.plasm-ph/1809.06007.

[10] B. Qiao, X. F. Shen, H. He, Y. Xie, H. Zhang, C. T. Zhou, S. P. Zhu, and X. T. He, Plasma Phys. Control. Fusion **61**, 014039 (2019).

[11] S. C. Wilks, A. B. Langdon, T. E. Cowan, M. Roth, M. Singh, S. Hatchett, M. H. Key, D. Pennington, A. MacKinnon and R. A. Snavely, Phys. Plasmas **8**, 542 (2001).

[12] H. Schwoerer, S. Pfotenhauer, O. Jäckel, K.-U. Amthor, B. Liesfeld, W. Ziegler, R. Sauerbrey, K. W. D. Ledingham, and T. Esirkepov, Nature (London) **439**, 445 (2006).

[13] K. Zeil, S. D. Kraft, S. Bock, M. Bussmann, T. E. Cowan, T. Kluge, J. Metzkes, T. Richter, R. Sauerbrey, and U. Schramm, New J. Phys. **12** 045015 (2010).

[14] M. Gauthier, C. B. Curry, S. Göde, F.-E. Brack, J. B. Kim, M. J. MacDonald, J. Metzkes, L. Obst, M. Rehwald, C. Rödel et al., Appl. Phys. Lett. **111**, 114102 (2017).

[15] T. Esirkepov, M. Borghesi, S. V. Bulanov, G. Mourou, and T. Tajima, Phys. Rev. Lett. **92**, 175003 (2004).

[16] A. P. L. Robinson, M. Zepf, S. Kar, R. G. Evans, and C. Bellei, New J. Phys. **10**, 013021 (2008).

[17] B. Qiao, M. Zepf, M. Borghesi, and M. Geissler, Phys. Rev. Lett. **102**, 145002 (2009).

[18] A. Macchi, S. Veghini, and F. Pegoraro, Phys. Rev. Lett. **103**, 085003 (2009).

[19] S. Kar, K. F. Kakolee, B. Qiao, A. Macchi, M. Cerchez, D. Doria, M. Geissler, P. McKenna, D. Neely, J. Osterholz et al., Phys. Rev. Lett. **109**, 185006 (2012).

[20] A. Sgattoni, S. Sinigardi and A. Macchi, Appl. Phys. Lett. **105**, 084105 (2014).

[21] C. Scullion, D. Doria, L. Romagnani, A. Sgattoni, K. Naughton, D. R. Symes, P. McKenna, A. Macchi, M. Zepf, S. Kar et al., Phys. Rev. Lett. **119**, 054801 (2017).

[22] X. F. Shen, B. Qiao, H. Zhang, S. Kar, C. T. Zhou, H. X. Chang, M. Borghesi, and X. T. He, Phys. Rev. Lett. **118**, 204802 (2017); X. F. Shen, B. Qiao, H. X. Chang, W. D. Zhang, H. Zhang, C. T. Zhou, and X. T. He, New J. Phys. **19**, 033034 (2017).

[23] F. Pegoraro and S. V. Bulanov, Phys. Rev. Lett. **99**, 065002 (2007).

[24] M. Nisoli, S. De Silvestri, and O. Svelto, Appl. Phys. Lett. **68**, 2793 (1996).

[25] D. Herrmann, L. Veisz, R. Tautz, F. Tavella, K. Schmid, V. Pervak and F. Krausz, Opt. Lett. **34**, 2459 (2009).

[26] Z. Major, S. A. Trushin, I. Ahmad, M. Siebold, C. Wandt, S. Klingebiel, T. J. Wang, J. A. Fülop, A. Henig, S. Kruber et al., Rev. Laser Eng. **37**, 431 (2009).

[27] S. Bohman, A. Suda, T. Kanai, S. Yamaguchi, and K. Midorikawa, Opt. Lett. **35**, 1887 (2010).

[28] M. Tamburini, A. Di Piazza, T. V. Liseykina, and C. H. Keitel, Phys. Rev. Lett. **113**, 025005 (2014).

[29] S. Kühn, M. Dumergue, S. Kahaly, S. Mondal, M. Füle, T. Csizmadia, B. Farkas, B. Major, Z. Várallyay, E. Cormier, M. Kalashnikov, et al., J. Phys. B At. Mol. Opt. Phys. **50**, 132002 (2017).

[30] L. Di Lucchio, A. A. Andreev and P. Gibbon, Phys. Plasma **22**, 053114 (2015).

[31] M. L. Zhou, X. Q. Yan, G. Mourou, J. A. Wheeler, J. H. Bin, J. Schreiber, and T. Tajima, Phys. Plasma **23**, 043112 (2016).

[32] D. Kormin, A. Borot, G. J. Ma, W. Dallari, B. Bergues, M. Aladi, I. B. Földes and L. Veisz, Nat. Commun. **9**, 4992 (2018).

[33] A. P. L. Robinson, A. V. Arefiev and D. Neely, Phys. Rev. Lett. **111**, 065002 (2013).

[34] V. V. Kulagin, V. A. Cherepenin, M. S. Hur and H. Suk, Phys. Rev. Lett. **99**, 124801 (2007).

[35] T. D. Arber, K. Bennett, C. S. Brady, A. Lawrence-Douglas, M. G. Ramsay, N. J. Sircobe, P. Gillies, R. G. Evans, H. Schmitz, A. R. Bell, and C. P. Ridgers, Plasma Phys. Control. Fusion **57**, 113001 (2015).

[36] M. V. Ammosov, N. B. Delone, and V. P. Krainov, Sov. Phys. JETP **64**, 1191 (1986).

[37] A. Taflove and S. C. Hagness, Computational Electrodynamics: The Finite-Difference Time-Domain Method. Artech House, 2000.

[38] M. Tamburini, F. Pegoraro, A. Di Piazza, C. H. Keitel, and A. Macchi, New J. Phys. **12**, 123005 (2010).

[39] H. B. Zhuo, Z. L. Chen, W. Yu, Z. M. Sheng, M. Y. Yu, Z. Jin, and R. Kodama, Phys. Rev. Lett. **105**, 065003 (2010).

[40] D. J. Stark, L. Yin, B. J. Albright, and F. Guo, Phys. Plasmas **24**, 053103 (2017).

[41] H. Y. Wang, C. Lin, Z. M. Sheng, B. Liu, S. Zhao, Z. Y. Guo, Y. R. Lu, X. T. He, J. E. Chen, and X. Q. Yan, Phys. Rev. Lett. **107**, 265002 (2011).

[42] J. H. Bin, W. J. Ma, H. Y. Wang, M. J. V. Streeter, C. Kreuzer, D. Kiefer, M. Yeung, S. Cousens, P. S. Foster, B. Dromey, X. Q. Yan et al., Phys. Rev. Lett. **115**, 064801 (2015).

(a) Legend: $6^*n_h$, $n_e$, $10^*n_b$, $F_x$, $E_L/3$. Electron sheet. Axes: $n/n_c$, $E_x/E_0$, $x/\lambda$.

(b) Inset: $p_i/m_ic$ vs $x/\lambda$. Axes: $n/n_c$, $E_x/E_0$, $x/\lambda$.

(c) Bunched protons. Axes: $n/n_c$, $E_x/E_0$, $x/\lambda$.

(d) Legend: $\tau_L = 1T0$, $\tau_L = 2T0$, $\tau_L = 3T0$. Axes: $dN/dE$, En [MeV].

(a) Capacitor-like field $E_x$ / $z/\lambda$ / $E_y$ / $x/\lambda$

(b) Carbon ions / Protons / Electrons / $E_x$ / $y/\lambda$ / Backward electrons / $E_y$ / $x/\lambda$

(c) RPA / $\tau_L = 3T_0$ / $2T_0$ / $1T_0$ / Proton / Carbon / $dN/dE$ / $E_n[MeV/u]$

(a) Graph with x-axis labeled $a_0$ and y-axis labeled "Optimal thickness (nm)". Annotation: $1 \approx a_0 n_c \lambda T_0 / 4\pi n_e \gamma_L$. Legend: ✳ 2D simulation, — Theory prediciton.

(b) Graph with x-axis labeled "Laser energy (J)" and y-axis labeled "Peak Energy (MeV)". Annotations: $\epsilon \sim \xi_L^{0.6}$, $\epsilon \sim \xi_L$. Legend: ✳ 2D simulation, + 3D simulation.